Characterization of 3-strap antennas in ASDEX Upgrade

Original
Characterization of 3-strap antennas in ASDEX Upgrade / Bobkov, Volodymyr; Bilato, Roberto; Colas, Laurent; Dux, Ralph; Faudot, Eric; Faugel, Helmut; Fã¼nfgelder, Helmut; Herrmann, Albrecht; Jacquot, Jonathan; Kallenbach, Arne; Milanesio, Daniele; Maggiora, Riccardo; Neu, Rudolf; Noterdaeme, Jean-Marie; Ochoukov, Roman; Pã¼tterich, Thomas; Tierens, Wouter; Zhang, Wei. - In: EPJ WEB OF CONFERENCES. - ISSN 2101-6275. - STAMPA. - 157:(2017), p. 03005. (22nd Topical Conference on Radio-Frequency Power in Plasmas 2017 Aix-en-provence May 30 - June 2, 2017) [10.1051/epjconf/201715703005].

Publisher:
EDP Sciences

Published
DOI:10.1051/epjconf/201715703005

Journal of Intelligent and Robotic Systems manuscript No.
(will be inserted by the editor)

Ground risk map for Unmanned Aircraft in Urban Environments

Stefano Primatesta · Alessandro Rizzo ·
Anders la Cour-Harbo

Received: date / Accepted: date

Abstract The large diversity of unmanned aircraft requires a suitable and proper risk assessment. In this paper, we propose the use of risk map to define the risk associated to unmanned aircraft. It is a two-dimensional location-based map that quantifies the risk to the population on ground of flight operations over a specified area. The risk map is generated by a probabilistic approach and it combines several layers, including population density, sheltering factor, no-fly zones, and obstacles. Each element of the risk map has associated a risk value that quantifies the risk of flying over a specific location. Risk values are defined by a risk assessment process using different uncontrolled descent events, drone parameters, environmental characteristics, as well as uncertainties on parameters. The risk map is able to quantify the risk of large areas, such as urban environments, and allows for easy identification of which locations the flight has high and low risk. The map is a tool for informed decision making, and results report some examples of risk map with different aircraft in a realistic urban environment.

Keywords unmanned aerial vehicles · unmanned aircraft · risk map · risk assessment · aviation safety · probability of fatality

---

S. Primatesta
Department of Control and Computer Engineering, Politecnico di Torino, Corso Duca degli Abruzzi 24, 10129 Torino, Italy
E-mail: stefano.primatesta@polito.it

A. Rizzo
Department of Electronics and Telecommunications, Politecnico di Torino, Corso Duca degli Abruzzi 24, 10129 Torino, Italy

A. la Cour-Harbo
Department of Electronic Systems, Aalborg University, Frederik Bajers Vej 7C, 9220 Aalborg East, Denmark

1 Introduction

The diversity of Unmanned Aircraft Systems (UASs) in our society is growing. UASs are used in a wide range of applications, both in military and civil fields. In particular, the use of UASs in urban environments will increase significantly in the near future, for instance as described in Smart Cities [44,37].

While the technology of unmanned aircraft is developing rapidly, the safety associated with their operations is not growing equally fast. At the moment, the use of a UAS requires the flight authorization from the National aviation agency, obtained if a certain level of safety is guaranteed. National aviation authorities, such as the ENAC (Ente Nazionale per l'Aviazione Civile) in Italy, or the FAA (Federal Aviation Administration) of the United States provide particular rules of lightweight UASs and, at the moment, most of the operations must be performed in Visual Line-Of-Sight (VLOS). However, they are opening the possibility to perform Beyond Visual Line-Of-Sight (BVLOS) flight for specific operations. In particular, the European Aviation Safety Agency (EASA) publishes a proposal for legislation [26,27] for UASs in the European airspace. They adopted the Joint Authorities for Rulemaking on Unmanned Systems (JARUS) proposal, in which three risk-based categories of unmanned aircraft are identified: open, specific and certified. The importance of a risk-based approach is recognized by EASA and FAA and, for this reason, it is adopted to the development of a regulatory framework for unmanned aircraft [25].

Urban areas are a special case and current aviation regulations strongly limit the use of UASs in these areas. For a full exploitation of UASs in urban areas, a revision of aviation regulation is necessary. For an analysis of the worldwide regulation, see [7,54]. Recently, the FAA launched the UAS Integration Pilot Program (IPP), where BVLOS flight operations are tested in ten US cities [28].

Urban areas are critical environments because of the high population density. For this reason, in our risk-adverse society, it is mandatory to assess the risk to the population on ground. A realistic and detailed risk assessment is one of the major challenges, because it is not easy to quantify the effective risk of a particular flight mission. An efficient risk assessment can also help the authorities to quantify the risk level of a particular flight operation, guaranteeing a realistic level of safety.

1.1 Previous work

In literature, there are several works that aim to quantify and manage the risk of an unmanned aircraft. Most of them are inspired by manned aviation, where risk assessments have been conducted for decades [29]. With manned aviation the risk assessment and requirements are clearly defined ensuring an "Equivalent Level of Safety" (ELOS) [24]. On the contrary, the risk assessment and requirements of unmanned aerial vehicles are not defined as well.

1.1.1 Unmanned aircraft risk assessment

In the last years with the large diversity of the unmanned aerial vehicles, several works about the risk assessment and mitigation of the risk are conducted. In [10], a safety risk management process is described, discussing the high level safety criteria, the identification, analysis and evaluation of the risk, and the effectiveness of the available mitigation strategies. A Barrier Bow Tie Model (BBTM) is presented in [12] and used for risk assessment and decision-making activities, while in [58] a Bayesian approach is applied to perform a risk assessment and decision making processes, in order to certificate UAS according to regulation requirements. In [19], a safety architecture based on an extension of borrow tie diagrams is proposed, whereas in [41] a risk criteria for UAS is presented, analyzing the safety, hazard and risk metrics. Another work in [1] presents a real-time risk assessment framework to provide real-time safety evaluation and tracking.

In [11], the authors describe a risk analysis for UAS, where the risk to people and property on ground is analyzed. Similarly, in [17] a complete risk assessment approach is described, analyzing the UAS accidents and their fatality rate. The authors introduce a model to estimate the probability of fatality of people exposed to the impact on ground. In [15] the author presents a complete probabilistic risk assessment method, where different descent event types are considered, as well as uncertainties on the parameters and the wind effect. In [33] the impact area of a generic descent is studied, considering also a buffer area, while in [42] a casualty prediction model for UAS operation is described.

The above-mentioned works [11,15,17,42] are based on a common probabilistic risk assessment method, where the risk is defined as the probability to cause a fatality per flight hours. The probabilistic risk assessment is also used to quantify the risk related to flight operations. In [4], an high fidelity approach is used to quantify the risk. In [16], the high fidelity probabilistic approach is compared with the Specific Operations Risk Assessment (SORA), proposed by JARUS in [36] and adopted by EASA. For a wide review of the state of the art about ground risk modeling of unmanned aircraft, see [57].

1.1.2 Descent models

In order to determine the risk of an unmanned aircraft, it is necessary to estimate the behavior of the aircraft descent. Generally, a fatality occurs after the uncontrolled impact of the unmanned aircraft on the ground. However, the type of the vehicle and the descent event type influence the nature of the impact distribution.

In [15], the author uses four descent event types: ballistic descent, uncontrolled glide, parachute descent and fly away. In particular, the same author in [13] proposes the model of the ballistic descent of small unmanned aircraft.

In [4], the fatality happens after a power failure, then, it assumes the uncontrolled glide descent.

The impact area can be estimated also using simulations of the unmanned aircraft in uncontrolled descent, such as in [34,59]. In [55], trajectories of explosive debris are studied, estimating the impact point given the initial condition.

1.1.3 Risk maps

The risk map is a common tool in the risk assessment. Risk maps are used in a lot of research areas, such as in medicine to estimate the areas effected by epidemics [56], to estimate the risk of accidents of nuclear power plants [2], as well as to quantify and manage the risk in financial and business field [21].

However, there are few works in literature that use the risk map to quantify the risk of UAS. In [18], a risk map is associated with the ground orography to minimize the risk of collisions. In [31,48] a risk map quantifies the risk to the population on ground, in order to compute the minimum risk path.

However, none of the above-mentioned works use the risk assessment method for generate a city wide map, quantifying the risk of an entire urban area. Moreover, works in [31,48] compute a ground risk map using the approach described in [32,33], where the area exposed to the crash is computed only using the dimension of the aircraft and a fixed glide angle set equal to 45° for fixed wing aircraft and 90° for multi-rotor. Thus, the impact area is not estimated considering the traveling distance of the aircraft when the failure occurs, as well as different descent events and uncertainties are not taken into account.

1.1.4 Risk-aware path planning

The risk assessment can be used to provide a safe robot navigation. In particular, risk-aware path planning is a common problem in robotics. In [18,31,48] a risk-aware path planning seeks for the minimum risk path for unmanned aircraft based on risk maps. Similarly, in [51] the authors use a bi-objective optimization method to find low-risk and time solution for UAVs in urban environments.

A risk-based path planning is also used to seek for a safe landing place [8,43].

1.2 Current work

In this work, we propose a tool for the risk assessment for ensuring risk-informed decision making. The main contribution is the definition of a risk map that quantifies the risk to the population on ground, when the UAS flies over a specific area. It takes into account the drone parameters and the environment characteristics, as well as uncertainties on parameters and wind. The risk is computed using various descent event types, such as the ballistic descent, the uncontrolled glide, parachute descent and fly away. It includes also no-fly zones and obstacles at the flight altitude.

In order to generate a suitable map, a detailed risk analysis is proposed. It is based on the probabilistic risk assessment method used in [11, 15, 17]. Inspiring to [15], it takes into account the drone specifications, the characteristics of the environment and uncertainties on the model. The descent of the unmanned aircraft is modeled using the method proposed in [13, 15], as well as the wind effect on the ground impact area. Moreover, unlike [13, 15], we consider also probabilistic assumptions on flight direction and altitude. Thus, based on the risk analysis, a risk map is generated.

The basic principle of the risk map described in this paper has been introduced in [47], as a part of a Cloud-based framework for risk-aware intelligent navigation in urban environments. Moreover, as a part of the same project, a preliminary version of risk map is used in [48] to perform a risk-aware path planning.

Generally, the probabilistic risk assessment approach in [11, 15, 17] is used to quantify the risk of a pre-determined flight mission. On the contrary, the risk map is a very promising tool, and it can be used in a wide range of applications. It can be helpful to quantify and show the effective risk of fly over a specific city. It can be also used to planning a low risk mission or to modify a flight mission, in order to reduce the risk.

Compared to [31, 48], the proposed risk map evaluates different descent event types, estimating the impact area with the traveled distance by the vehicle, as well as estimating impact velocities, kinetic energy and the glide angle at impact considering uncertainties and wind. It is very important to estimate the aircraft behavior at the descent, because the impact area may be very far from the position of the aircraft when the failure event occurs.

This paper is organized as follows. In Section 2 the main architecture of the risk map generation is presented, describing each layer used in the framework. Section 3 describes the risk assessment approach, describing all the descent event types considered. In Section 4 the final step for the risk map generation is described, with the merging layers procedure. Finally, Section 5 describes numerical results. Then, our conclusions are drawn in Section 6.

2 Risk map generation

The risk map is a cell-based map, in which each cell has a specific risk value. The risk map covers large predefined areas and takes into account drone specifications, flight direction and altitude, as well as characteristics of the environment and wind. The risk is defined as the probability to cause a casualty, considering different descent events. In next sections, more details about the risk map generation are reported.

2.1 Risk map

The risk map is a two-dimensional location based map quantifying the risk to people on the ground for each cell in the map. Cells are equidistantly dis-

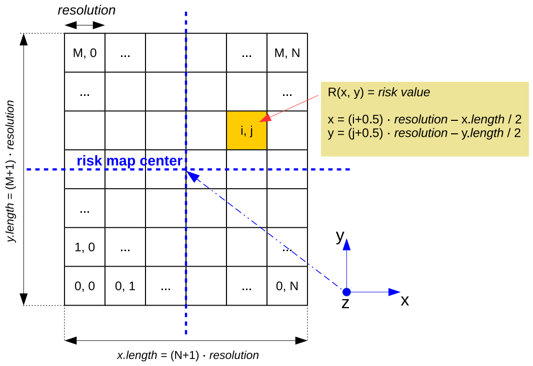

Fig. 1 Representation of the risk map and the associated notation.

tributed and square and each represents a geographical area. The entire map is represented by a matrix of size $N \times M$ cells, called $\mathbf{R}$. As such, each cell $\mathbf{R}(i, j)$ is an element called risk value, which is the risk for the associated geographical area. The discrete coordinates (i, j) represent a georeferenced location (x, y) in the Local NED coordinate system defined with respect to the reference frame located in the center of the map. With a slight of abuse of notation, in this paper we use the notation $\mathbf{R}(x, y)$ to indicate the cell of the risk map centered in the location (x, y), but corresponding to some discrete coordinates (i, j) of the matrix $\mathbf{R}$. Figure 1 clarifies the representation of the risk map. When implementing the risk map computation in C++ code appropriate conversions between geographical (x, y) and matrix indices (i, j) are necessary. Such conversions are not discussed in this work.

Risk values are defined considering the risk level, no-fly zones and the presence of obstacles at the flight altitude.

Conceptually, the risk map is generated by combining several layers, where each layer is itself a location-based map containing the required data. Layers have the same characteristics as the risk map. In this work, the multilayer framework is composed by the following layers:

- **Population density layer** defines the population density distribution in the map.
- **Obstacles layer** defines the height of obstacles in the map.
- **Sheltering layer** defines the sheltering level of each cell of the map.
- **No-fly zone layer** defines in which zones the flight is not allowed.

The procedure for generating the risk map is illustrated in Figure 2. In particular, two main steps are executed. First, with the risk assessment, four maps are generated, one for each descent event taken into account. For simplicity they are called *event maps*. The inputs of the risk assessment are the population density and the sheltering factor layers, as well as drone parameters and environment characteristics. Event maps are preliminary risk maps where only the risk level associated with the descent event is expressed. Second, the

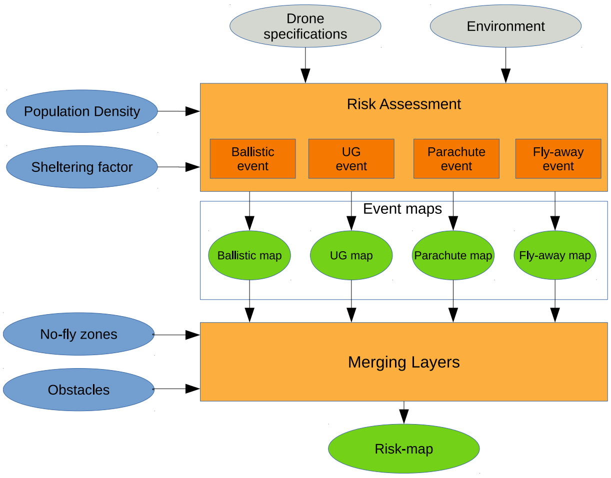

Fig. 2 The main architecture of the risk map generation.

final risk map is generated, by combining the event maps with no-fly zone and obstacles layers.

2.2 Population Density Layer

The population density layer defines the density of the population in the area interested by the risk map. The population density is one of the most important element in the risk assessment, because it describes how many people can be involved in the crash of the vehicle and how they are distributed on the map. In particular, the population density has effect on the probability to impact with a person on ground. For this reason, to perform a proper risk assessment, a population density grid with a reasonably fine resolution is mandatory.

Often the population density and distribution are collected by National statistical institutes and, especially in big cities, by municipalities. Collecting all the census data, in [23] the gridded population of the world is created with a resolution of 1 km^2. High resolution map can be obtained via dasymetric mapping and, in [52], a population density grid map for Europe is generated with a resolution of 100 × 100 m.

In urban areas, the population density can be estimated from Mobile phone data [38], a promising approach able to trace the dynamic distribution of people on ground [20]. In fact the population distribution of people in cities changes a lot in respect of the day of the week and of the times of the day.

Basically, in our framework the population density layer is a 2D location based map with the same dimension of the risk map, where each cell has associated a value corresponding to the population density at the relative position, expressed in people/m^2. Similarly to the risk map, it is represented as a matrix $\mathbf{D}$, with elements $\mathbf{D}(x, y)$. In this work a portion of the city of Turin

(Italy) is considered as example, thus, all the layers and map reported in this work are related to this area. Figure 3 illustrates the interested area with the realistic (but not real) population density with a resolution of 50×50 m. Turin is an interesting city to test the risk map, because it has an high population density with an average value of 6939 people/km^2 [35].

2.3 Obstacles Layer

The obstacles layer defines the height of obstacles in the map, such as buildings. Taking into account the model of the city, it is quite easy to define the obstacles layer. Practically, this layer is a location based map and, similarly to the risk map, it is represented as a matrix $\mathbf{O}$, where each cell $\mathbf{O}(x, y)$ quantifies the maximum height of buildings and/or objects in the associated location. The obstacles layer is not used in the risk assessment procedure, but it is used to determine no-flyable areas because of the presence obstacles at the flight altitude. Then, the probability of collision with obstacles is not taken into account. Anyway, the obstacles layer is also used to define the sheltering factor layer by evaluating all obstacles and buildings below the flight altitude.

In this work the obstacles layer is defined using the model of the city of Turin from OpenStreetMap (OSM) [46]. OSM is an open source map of the entire world. Using the OSM data, the tridimensional model of the city can be extracted, then the obstacles layer is generated. An example of the obstacles layer is illustrated in Figure 5.

2.4 Sheltering Factor Layer

The sheltering factor layer defines the sheltering level for each cell of the map. The sheltering factor is a positive number that quantifies the level of shelter to people in the area. It is very important to consider it, because the presence of buildings and other obstacles in the crash area of the UAS can reduce the kinetic energy at impact, and subsequently the probability of fatalities. If the sheltering factor is not evaluated, the resulting risk can be over-conservative, especially in urban environments where buildings, vehicles and trees protect the population. While the obstacles layer defines the height of the obstacles in the map, the sheltering factor layer quantifies the sheltering level of objects in the map. For instance, a building provides a greater sheltering level then a tree.

The definition of the sheltering factor used in this work is inspired by [17], where the sheltering factor is an absolute real number in the range from 0 to infinite, used as parameter in the Equation (8), that quantifies the probability to cause fatal injuries to people exposed to the crash. However, according to [32], it is useless to consider elevate values of the sheltering factor, because, after a certain value, it is required a huge kinetic energy to cause a casualty. Thus, according to [32], in this work we define the sheltering factor in the

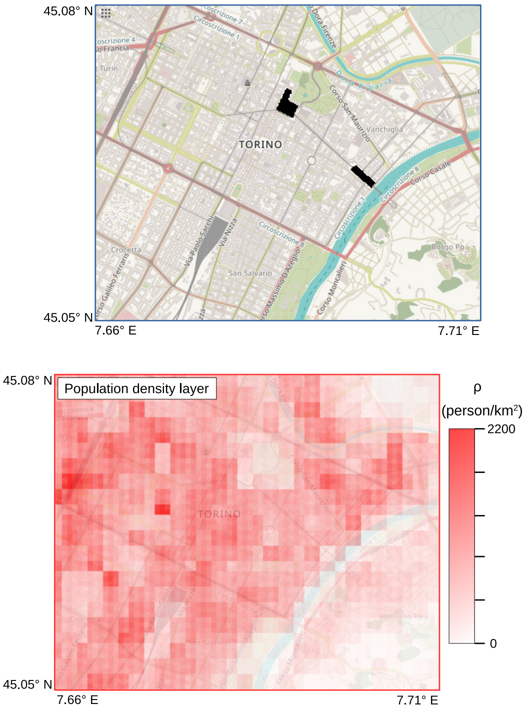

Fig. 3 On top the portion of city of Turin from OpenStreetMap [46] used in this work as example. The area comprises the city center and it has a dimension of about 4.05 × 3.52 km. Black areas are the imaginary no-fly zones defined in correspondence of the two main city center squares. Below, the imaginary population density layer used as example with a resolution of 50 × 50 m.

range from 0 to 10, where 0 corresponds to an area without shelter and 10 to an area with the maximum sheltering factor, such as an industrial building. For instance, using the Equation (8), with a kinetic energy of about 250 J and sheltering factor equal to 2 the probability to have a fatality after the impact with a person is 0.38. With the sheltering at 10, the probability decreases to 0.025. Table 1 reports the sheltering factor classification defined in this work.

In literature, the sheltering factor is also used to compute the probability of impact a person P_{impact} [15], rather than the probability to cause fatal injuries. Anyway, it is essential to consider it once, otherwise the contribution of the sheltering factor in the risk assessment is overestimate.

The sheltering factor layer is a location based map represented with a matrix $\mathbf{S}$, where each element $\mathbf{S}(x, y)$ assumes the sheltering factor value related to the corresponding location. In this work the sheltering factor layer is generated with a simple method. From the obstacles layer described in Section 2.3, it is associated a sheltering factor equal to 7.5 to areas occupied by buildings. Where we have no information about the sheltering, an average value of 2.5 is selected. This is a reasonable value, because, generally, people are sheltered

Table 1 Sheltering factor classification

Sheltering	Area
0	No obstacles
2.5	Sparse trees
5	Vehicles and low buildings
7.5	High buildings
10	Industrial buildings

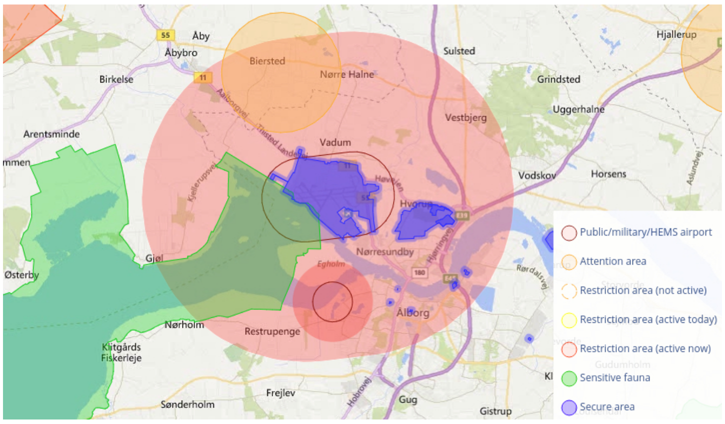

Fig. 4 Example of no-fly zones around the city of Aalborg, Denmark. The image is from [45], a website that shows both temporary and permanent restriction areas in Denmark.

by cars, trees and by low buildings. The sheltering factor layer used in this work is illustrated in Figure 5.

2.5 No-Fly Zone Layer

The no-fly zone layer is a map that identifies all the no-fly zones in the urban area. No-fly zones are typically determined by:

1. National regulation agencies, i.e. ENAC in Italy and FAA in the United States. No-fly zones are defined for safety reason and, often, they delimit airports and military areas.
2. Nature sensitive areas, such as National parks or other protected areas where the flight is not allowed.
3. Security zones are areas where the flight is not allowed because of generic safety reason. For instance, crowded zones in urban areas, such as main squares or areas with public events.
4. Zones defined by the operator as general not open for operations.

Figure 4 shows an example of no-fly zones imposed by the National aviation agency.

In our framework, the no-fly zone layer is a location-based map, in which each element can assume two values: 0 where the flight is allowed, and -1

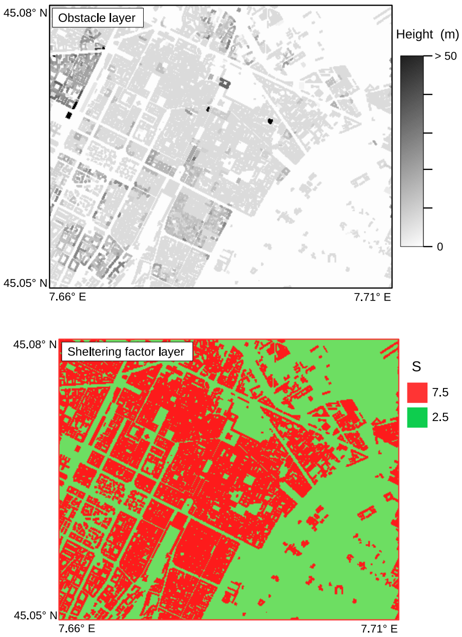

Fig. 5 On top the obstacles layer of Turin city center with a resolution of 10 × 10 m. The data are obtained from OSM [46]. Below, the sheltering factor layer with the same resolution of 10 × 10 m.

where the flight is forbidden. Similarly to the risk map, the no-fly zone layer is a matrix **F** as

$$\mathbf{F}(x,y)=\begin{cases}-1 & \text{flight is not allowed,}\\ 0 & \text{flight is allowed.}\end{cases}\tag{1}$$

In Figure 3, no-fly zones are highlighted over the map of the city, where two imaginary no-fly zones are defined over the two main city center squares.

3 Risk assessment description

In this work the risk is defined as the risk to the population on ground, when the UAS flies over a specific area. The risk value is computed with a common approach widely used in literature [11,15,17,33] and it is expressed in fatalities per flight hour, a classic measure system used in aviation. This is a probabilistic approach, where the risk value is the probability in time to have a casualty, due to a sequence of three conditional events: *(i)* the loss of control of the vehicle with uncontrolled crash on ground, *(ii)* the impact with a person after the crash, and *(iii)* the impact results in a fatality. Hence, the probability to have a casualty P_{casualty} is defined as

$$P_{\text{casualty}}(x,y)=P_{\text{event}}\cdot P_{\text{impact}}(x,y)\cdot P_{\text{fatality}}(x,y),\tag{2}$$

with P_{event} is the probability that the UAS losses the control with the consequent uncontrolled descent with crash on ground. The behavior of the uncontrolled descent event depends on the failure type. In this work, we consider four descent event types: ballistic descent, uncontrolled glide, parachute descent and fly-away. We assume a different P_{event} for each descent event and the independence between failures. For each descent type a mathematical model is used to determine the likely impact area, taking into account drone specifications and initial conditions. The ground impact area is described with a georeferenced two-dimensional probability density function (2D PDF), able to estimate the probabilistic impact area in respect to the aircraft position when the descent event begins. The descent models are described in [13,15]. More details are given in Sections 3.1 through 3.4.

P_{impact} is the probability to impact a person when the UAS crash on ground after an uncontrolled descent. It is function of the population density and the area exposed to the crash.

P_{fatality} is the probability to produce fatal injuries after a person has been impacted. It depends on the kinetic energy at impact and the sheltering factor.

In order to generate the event maps, P_{casualty} is computed for each descent event type and for every cell of the map. The computation of the risk value follows a common procedure:

1. Using the model of the descent event type, the two-dimensional PDF is computed, defining the probabilistic impact area on ground.
2. The PDF is modified by the probabilistic wind. The resulting two-dimensional PDF is transformed according to the wind speed and direction.
3. The 2D PDF is used to compute the probabilities P_{impact} and P_{fatality} by combining it with the population density, the sheltering factor layer and impact velocities.
4. The probability of casualty P_{casualty} is computed.

The two-dimensional PDF defines the ground impact area determining the probabilities to impact on ground. In this work, the 2D PDF is represented as a georeferenced matrix referring to the aircraft position when the descent event happens. Each element of the matrix represents a geolocation with associated the probability of the unmanned aircraft to impact inside the represented area. Since, the risk map quantifies the risk for large areas, the 2D PDF is computed for every element in the map, assuming that the descent event begins in the location (x, y). Also the 2D PDF refers to the risk map frame, defined in the center of the map.

Each element of the risk map $\mathbf{R}(x, y)$ quantifies the risk of the unmanned aircraft of flying over the location (x, y). However, the exact velocity and direction of the aircraft are unknown. For this reason, the two-dimensional PDF computed for each descent type uses probabilistic assumptions on velocity and direction. Any flight direction is taken into account, distributed as a uniform distribution. Instead, the velocity assumes two possible scenarios, based on the vehicle type. With fixed wing aircraft the cruise speed is used assuming uncertainties, modeled as a normal distribution $\mathrm{N}(\mu, \sigma)$, with a mean value μ

Fig. 6 The Heliscope Talon aircraft. Image from [40].

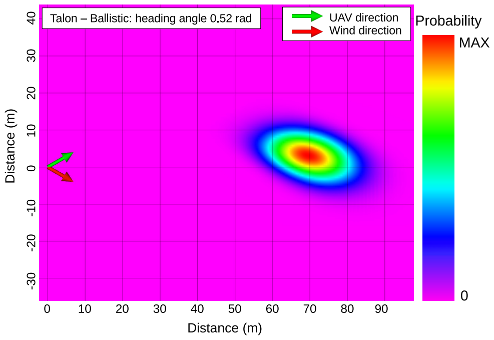

Fig. 7 A two-dimensional PDF of the ballistic descent event with the Talon aircraft. The red area is with highest probability, whereas the magenta area is with probability equal to zero. In this example the UAS flies at an altitude given as $N(\mu = 50, \sigma = 5)$ m, with a heading angle of 0.52 rad. The wind has a direction of -0.52 rad and speed $N(10, 2)$ m/s. The parameters of Talon aircraft are reported in Table 2.

and a standard deviation σ. With multi rotor configurations, we use values of velocities between zero and the maximum one, distributed as a uniform distribution $\mathrm{U}(a, b)$, where a and b define the range of the distribution. Thus, also the hovering is taken into account.

In the following sections all steps are described, as well as each descent event type considered in this work. Moreover, two different commercial aircraft are used to illustrate the behavior for each descent event: the Heliscope Talon aircraft and the DJI Phantom 4. The Heliscope Talon, shown in Figure 6, is a fixed-wing aircraft, while the DJI Phantom 4 [22] is a quadrotor aircraft, one of the most popular commercial drones. The main parameters are reported in Table 2.

3.1 Ballistic descent

The ballistic descent happens when the UAS loose most of its lift. As a consequence, the vehicle is subject to a ballistic descent, where the body is affected solely by gravity and drag force. In this work, the ballistic descent is modeled

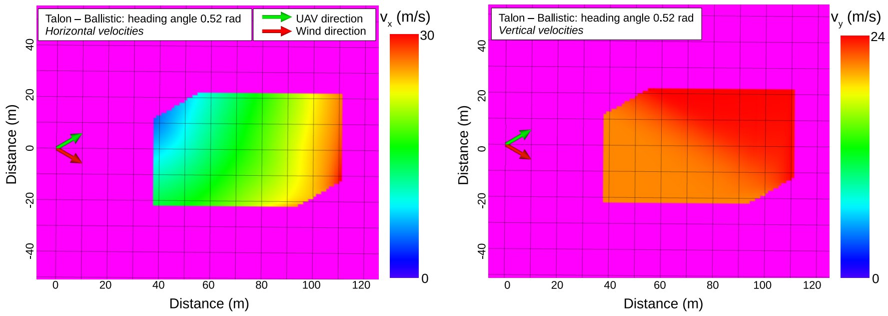

Fig. 8 On the left horizontal velocities of the ballistic descent event with the Talon aircraft, while on the right vertical velocities. Velocities are computed considering the area interested by the ballistic descent event, while the area where velocities are not computed are in magenta. Horizontal velocities are in the range from 8.32 m/s and 29.62 m/s, while the vertical velocities are in the range from 21.25 m/s to 23.96 m/s. These examples use the same parameters defined in Figure 7.

according to [13], where the model is based on the standard second order drag model

$$m\dot{\boldsymbol{v}} = mg - c|\boldsymbol{v}|\boldsymbol{v}, \tag{3}$$

with m is the mass of the UAS, c is the constant that considers the drag coefficient, drag area and the air density, g is the gravitational acceleration and v is the velocity vector of the vehicle. The ballistic trajectory is approximately a second order polynomial, taking into account the aerodynamic properties of the aircraft. The model presented in [13] also considers probabilistic uncertainties, as well as the wind.

The model is used to compute the two-dimensional probability density function with the probabilities of the UAS impact on ground. The PDF is computed considering probabilistic uncertainties on the horizontal and vertical initial velocities, on the drag coefficients, flight altitude and flight direction.

Moreover, according to the PDF, the horizontal and vertical impact velocities estimated by the model are stored in a 2D matrix. These are useful for the computation of the probabilities P_{impact} and P_{fatality}.

In Figure 7 an example of the two-dimensional PDF with a specific flight direction and velocity is illustrated. With the same scenario, Figure 8 reports impact velocities of the ballistic descent. Figure 9 shows the 2D PDF using a uniform distribution of all directions with both fixed wing and quad rotor configurations, used to generate the risk map.

3.2 Uncontrolled Glide

The uncontrolled glide event happens when the UAS enters in an uncontrolled descent governed by the glide ratio/autorotation descent angle. With a fixed wing aircraft, this event occurs when there's a loss of thrust or a loss of power

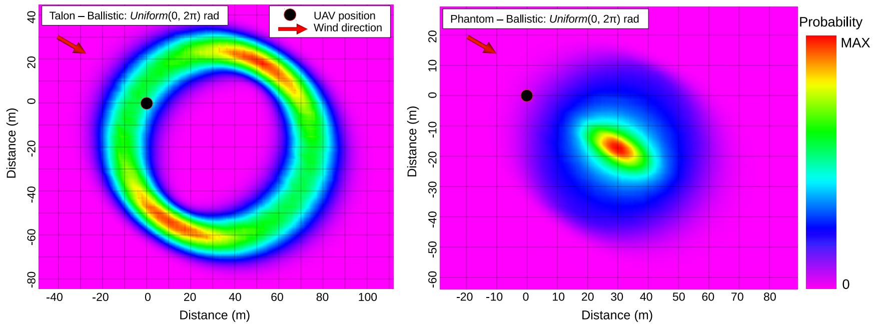

Fig. 9 On the left the 2D PDF of the ballistic descent with the Talon aircraft considering direction U$(0, 2\pi)$ rad and initial horizontal speed $N(18, 2.5)$ m/s. On the right the 2D PDF with the Phantom aircraft considering direction U$(0, 2\pi)$ rad and speed U$(0, 15)$ m/s. In this example the UAS flies at an altitude given as $N(50, 5)$ m. The wind has a direction of -0.52 rad and speed $N(10, 2)$ m/s.

for the flight control surfaces. For a single rotorcraft, it happens when there's a loss of thrust on the main rotor and the aircraft descent with autopiloted autorotation descent. Similarly, it could be happen with multi rotor drones, where a loss of thrust can cause an autopiloted descent.

With the uncontrolled glide event, the horizontal traveled distance is computed with the simple formulation $\text{dist}(h) = \gamma h$, with h is the flight altitude and γ is the glide ratio, i.e., the ratio between the horizontal traveled distance and vertical one.

The two-dimensional PDF of the uncontrolled glide event is computed with probabilistic assumption on the flight altitude, glide ratio, flight direction and velocities. As a consequence, the 2D PDF is related to the glide ratio distribution. The dynamics of the glide ratio in the PDF is stored in a 2D matrix, useful to estimate the impact angle in the probability density function.

Figure 10 illustrates the 2D PDF given a specific flight direction and velocity, while the glide ratio distribution is reported in Figure 11. Figure 12 shows the 2D PDFs considering all direction, used to generate the risk map.

3.3 Parachute descent

The parachute descent event happens when the UAS begins a descent with a fully deployed parachute. In general, a malfunction is detected, thus motors are turned off and the parachute is opened. However, a short delay is present between the emergency detection and the fully open of the parachute. The consequent descent is governed only by the aerodynamic properties of the parachute, which aims to reduce the vertical velocity. This event is modeled using the method presented in [15], where it considers the mass of the vehicle, as well as the physical parameters of the parachute, such as the parachute area and the parachute drag coefficient.

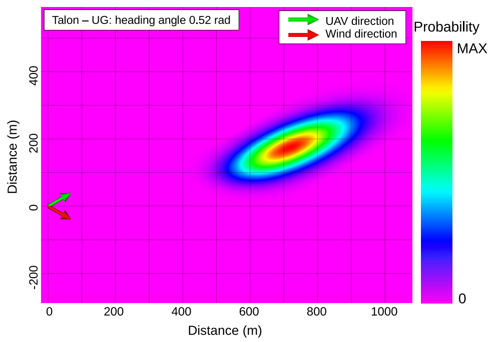

Fig. 10 The 2D PDF of the uncontrolled glide event with the Talon aircraft. This example uses the same parameters defined in Figure 7.

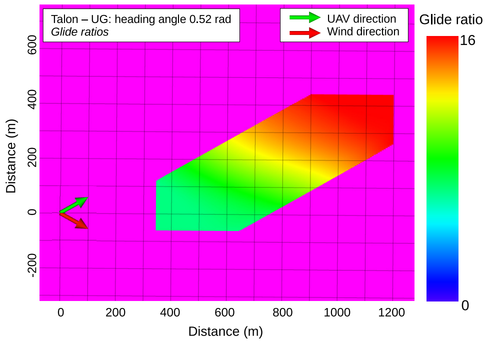

Fig. 11 The glide ratio distribution with the uncontrolled glide event with the Talon aircraft. The glide ratio is in the range from 8 to 16. In magenta, areas where the glide ratio is not computed. This example uses the same parameters defined in Figure 7.

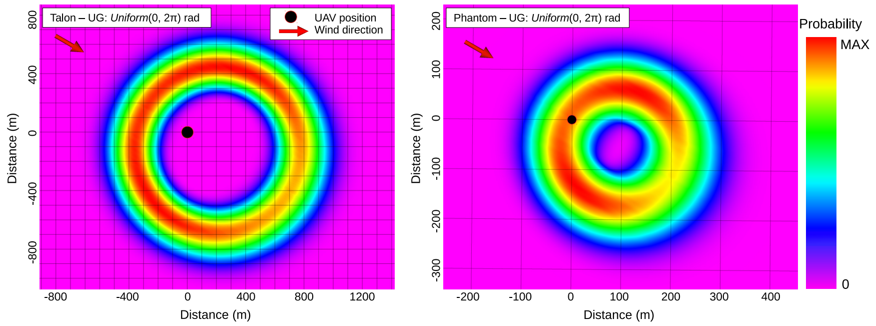

Fig. 12 On the left the 2D PDF of the uncontrolled glide event with the Talon aircraft, while on the right with the Phantom aircraft. These examples use the same parameters defined in Figure 9.

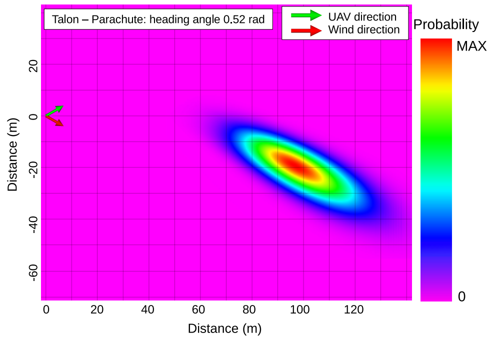

Fig. 13 The 2D PDF of the parachute descent with the Talon aircraft. This example uses the same parameters defined in Figure 7.

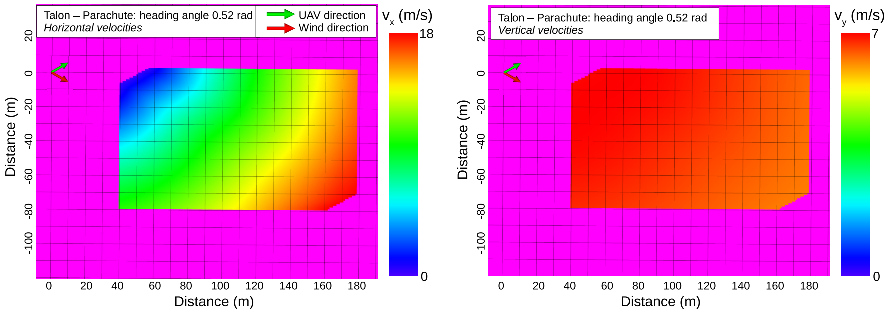

Fig. 14 On the left horizontal velocities of the Talon aircraft with the parachute descent, while on the right vertical velocities. Horizontal velocities are in the range from 2.74 m/s and 17.65 m/s, while vertical velocities are in the range from 6.15 m/s to 6.82 m/s. In magenta, areas where the impact velocities are not computed. These examples use the same parameters defined in Figure 7.

In particular, with this event the effect of wind drastically changes the effect of the parachute descent, by changing the descent direction and velocity.

The two-dimensional PDF is computed taking into account probabilistic assumption on the flight altitude, on the parachute drag coefficient, as well as on initial velocities. Similarly to the ballistic descent event, also the maps related to the horizontal and vertical velocities are computed and stored in a 2D matrix.

In Figures 13, 14 and 15, results of the parachute descent event are shown.

3.4 Flyaway

The flyaway event happens when there is a complete loss of operator control authority, while the autopilot on board maintains the vehicle stable. As a consequence, the UAS may flight in any direction as long as the autonomy of the vehicle be exhausted or until the UAS crashes on ground. This event

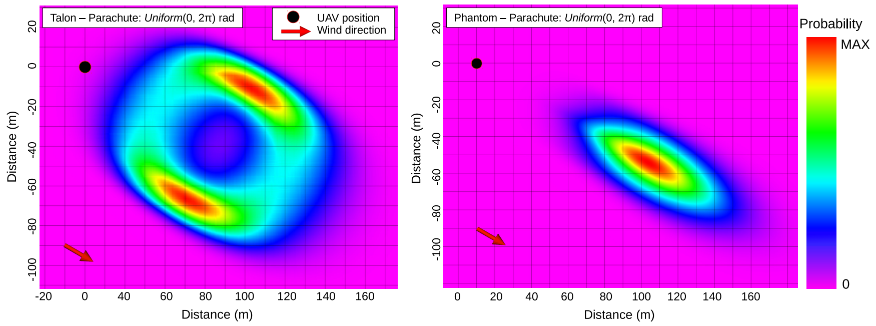

Fig. 15 On the left the 2D PDF of the parachute descent event with the Talon aircraft, while on the right with the Phantom aircraft. These examples use the same parameters defined in Figure 9.

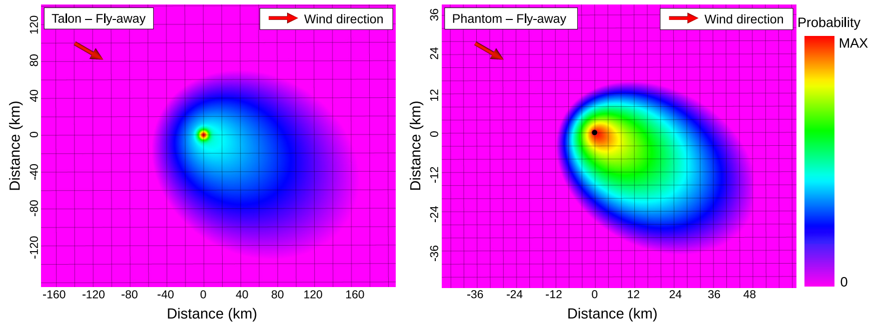

Fig. 16 Example of 2D PDF with the fly away event. On the left with the Talon aircraft, while on right with the Phantom aircraft. These examples use the same parameters defined in Figure 7.

is modeled according to [15], where the author proposes a model composed by two contributions: *(i)* the probability of the impact on ground decreases linearly with the distance from the UAS position until the maximum traveled distance of the vehicle; *(ii)* the vehicle moves vertically and the probability of ground impact is greater near the UAS position, then it is modeled as a normal distribution with the mean value in the UAS position. The two contributions are linearly combined with a relation factor. In this work, we assume that the two scenarios contribute with equal probability.

In order to be conservative, we assume that the fly away event terminates with an uncontrolled glide descent. Unlike the others descent events, the fly away always considers all direction because of its particular behavior. Figure 16 reports the results of the fly away event.

3.5 Wind

The wind is a very important factor in this work, because the effect of the wind changes significantly the two-dimensional PDF.

The features of the wind can be defined using the weather reports. In fact, if the day and time of the flight mission are known, the risk assessment procedure is able to consider wind characteristics estimated by the weather reports. Thus, the wind direction and speed are known and the wind is modeled with a normal distribution on direction and speed.

The models for the ballistic descent, uncontrolled glide and parachute descent are computed in the wind frame. These models provide a series of drop times, i.e. the time required by the aircraft to reach the ground given specific initial conditions. The set of all possible drop times are defined as $\{t_k\}_{k=0,\ldots,n}$, where for each drop time a georeferenced PDF is generated, defined as a matrix $\mathbf{M}_k$, where each element is a geolocation with associated the probability of the aircraft to impact inside the represented area, assuming a purely vertical drop in the wind frame. The offset caused by the wind is dependent only on the drop times, because all others parameters are already considered by the descent model. For this reason, the wind offset is applied to the georeferenced ground grid of each PDF with an horizontal translation determined as the drop time times the wind velocity. The drop times are computed with probabilistic assumptions on parameters, thus, a set of probabilities $\{p_k\}_{k,\ldots,n}$ define the probability of each drop time. Hence, the final 2D PDF is computed with a weighted sum of the PDF matrices as

$$\mathbf{M} = \sum_{k=0}^{n} p_k \mathbf{M}_k, \tag{4}$$

where the resulting matrix $\mathbf{M}$ is also georeferenced, taking into account the georeference of each matrix $\mathbf{M}_k$.

Differently, the fly away event is not computed in the wind reference frame, but directly in the local NED coordinate system in respect to the risk map reference frame. With the fly away, the wind simply modifies the maximum range of the distance traveled in different direction by the vehicle.

More details about the wind effect on the four descent events types are explained in [15].

The effect of the wind is reported in Figures 7, 8, 9, 10, 11, 12, 13, 14, 15 and 16. The effect of the wind is visible especially with the ballistic and parachute descent events, where the two-dimensional PDF is clearly deformed by the wind.

3.6 Probability of Impacting a Person

The probability of impact a person P_{impact} is the probability that the UAS hits at least one person after the uncontrolled impact on ground. According to several works at the state of the art [17,11], the probability is defined as

$$P_{\text{impact}}(x,y) = \rho(x,y) \cdot A_{\text{exp}}, \tag{5}$$

where ρ is the population density and A_{exp} is the area exposed to the crash, also known as *lethal area*.

The area exposed to the crash of the UAS on the ground is computed using the method proposed in [53], considering the dimension of the UAS and of an average person

$$A_{\text{exp}}(\theta) = 2(r_{\text{p}} + r_{\text{uav}})\frac{h_{\text{p}}}{\tan(\theta)} + \pi(r + r_{\text{p}})^2, \tag{6}$$

with r_{p} and h_{p} are respectively the average radius and height of a person, r_{uav} is the radius of the vehicle and θ is the impact angle on ground. With this formula, the computation of the area is conservative, because it uses the occupation of the vehicle with the maximum radius r_{uav}.

All the parameters of the Equation (6) are constant with the except of the impact angle θ. In fact the impact angle assumes different values based on the descent event.

With the ballistic and the parachute descent events the impact angle can be computed using horizontal and vertical impact velocities. As mentioned in Sections 3.1 and 3.3, the impact velocities are stored in a 2D matrix according to the 2D PDF.

Differently, in the uncontrolled glide and fly away events the impact angle depends directly on the glide ratio, as described in Section 3.2.

Thus, the probability of impact a person P_{impact} is computed using the expected value of the exposed area and the expected value of the population density in the layer **D** based on the ground impact PDF

$$P_{\text{impact}}(x,y) = \sum_{x,y} \text{PDF} \cdot \mathbf{D}(x,y) \cdot A_{\text{exp}}(\theta(x,y)), \tag{7}$$

where $A_{\text{exp}}(\theta)$ and **D** are independent variables.

The expected value is easily computed considering the probabilistic impact area, with a simple combination between the 2D PDF and layer, both defined as matrices. However, they have different dimension and resolution, but both matrices refer to the same risk map reference frame. Thus, each element of the PDF is combined with the element of the layer at the represented geolocation (x,y). This procedure is used in Equations (7), (9) and (10).

3.7 Probability of fatality

The probability of fatality P_{fatality} is the probability that the impact with a person results in a fatality.

It is not simple to define this probability, because the impact with a person may occur in several ways. The consequences of the impact depend on the properties of the vehicle. Moreover the human body reacts in different ways according to the hit part of the body and the kinetic energy at impact. In some works, the probability to have a casualty after an impact with a person is set equal to one [1,11]. However, this assumption can be over conservative, especially with small UAS.

For this reason, the definition of a realistic and proper probability of fatality is a challenge and there are several work in literature [3]. Interesting work in [14] analyzes the drone-like human injuries, identifying the mass threshold to consider the drone as an "harmless" one.

A common and widely used approach are the blunt criterion (BC) [5,9], but it is not suitable with low impact velocities.

In this work, the probability to have a fatality is computed using the method proposed in [17], considering the kinetic energy at impact and the sheltering factor. In particular, it is important to use the sheltering factor, because the presence of obstacles in the impact area reduces the kinetic energy at impact. As a consequence, the probability of fatality decreases significantly.

Similarly to the computation of the P_{impact}, the two-dimensional PDF is used to compute the expected value of the sheltering factor and the kinetic energy at impact for each position (x, y). Hence

$$P_{\mathrm{fatality}}(x,y) = \frac{1-k}{1-2k+\sqrt{\frac{\alpha}{\beta}}\left[\frac{\beta}{\mathsf{E}[E_{\mathrm{imp}}(x,y)]}\right]^{\frac{3}{\mathsf{E}[\mathrm{S}(x,y)]}}}, \tag{8}$$

with $k = \min[1, (\frac{\beta}{\mathsf{E}[E_{\mathrm{imp}}(x,y)]}^{\frac{3}{\mathsf{E}[\mathrm{S}(x,y)]}]})]$. Where S is the sheltering factor, E_{imp} is the kinetic energy at impact, the α parameter is the impact energy for a fatality probability of 50% when $\mathrm{S} = 6$, and the β parameter is the impact energy to cause a fatality when S goes to zero. In general, based on the fatality limit defined in [50], $\beta = 34J$. The notation $\mathsf{E}[\cdot]$ refers to the expected value. Hence

$$\mathsf{E}[E_{\mathrm{imp}}(x,y)] = \sum_{x,y} \mathrm{PDF} \cdot E_{\mathrm{imp}}(x,y), \tag{9}$$

$$\mathsf{E}[\mathbf{S}(x,y)] = \sum_{x,y} \mathrm{PDF} \cdot \mathbf{S}(x,y). \tag{10}$$

While the sheltering factor is obtained by the sheltering factor layer, the kinetic energy impact is estimated based on the descent event type.

In the ballistic and parachute descent events, the kinetic energy at impact is computed by horizontal and vertical impact velocities. Differently, with the uncontrolled glide and fly away events glide velocities are taken into account. However, the kinetic energy is computed with a simple formulation

$$E_{\mathrm{imp}}(x,y) = \frac{1}{2} m \cdot v_{\mathrm{imp}}(x,y)^2, \tag{11}$$

with m the mass of the vehicle and v_{imp} the impact velocity.

4 Merging Layers Procedure

After the risk assessment, the resulting event maps are merged with the no-fly zone and the obstacles layers, in order to have the final risk map. This procedure performs an element per element combination. Hence

$$\mathbf{R}(x,y) = \begin{cases} -1 & \text{if } \big(\mathbf{F}(x,y) = -1\big) \vee \big(\mathbf{O}(x,y) \geq h\big), \\ P_{\text{casualty}}(x,y) & \text{otherwise.} \end{cases} \tag{12}$$

where (x, y) are the coordinates of the element in the map, referred to the risk map reference frame. Each element of the risk map has a value $\mathbf{R}(x, y)$ equal to -1 if the flight is forbidden because of no-fly zones or obstacles at the flight altitude h, otherwise, it corresponds to the sum of the risk levels of each descent event

$$P_{\text{casualty}}(x,y) = P^{\text{bal}}_{\text{casualty}}(x,y) + P^{\text{ug}}_{\text{casualty}}(x,y) + P^{\text{par}}_{\text{casualty}}(x,y) + P^{\text{fa}}_{\text{casualty}}(x,y). \tag{13}$$

Since we assume the independence between descent events, the probabilities are simply added. The resulting $P_{\text{causalty}}(x, y)$ quantifies the risk involved by the aircraft when it flies over the element in the location (x, y).

After this procedure the risk map is generated. The resulting map quantifies the risk to the population considering a specified area, taking into account the flight altitude and the vehicle specifications. Moreover, it defines in which elements the flight is forbidden, because of no-fly zone or the presence of obstacles at the flight altitude.

5 Results and discussion

5.1 Implementation

The risk map generation procedure introduced in this paper is implemented in C++ as an executable process in the Robot Operating System (ROS) [49]. The multilayer framework is generated using Grid Map [30], a C++ library interfaced with ROS able to manage two-dimensional grid maps with multiple data layers. The computation of each two-dimensional PDF is performed using the OpenCV library [6], able to provide fast matrix computation. Moreover, the compatibility between OpenCV and GridMap allows an easy combination of the 2D PDF, defined as a OpenCV matrix, with layers and event maps, defined as GridMap layers, i.e. matrices.

In order to generate a realistic risk map, we consider a portion of the city of Turin, Italy. Then, each layer is generated as described in Section 2. Figures 3 and 5 show the portion of the city considered and the related layers.

In order to demonstrate how the risk changes with the vehicle characteristics, different aircraft types are taken into consideration, which differ on vehicle configuration type, mass and dimensions. Table 2 reports the vehicles with the main features and parameters used in the risk map generation. The

Table 2 Parameters of the aircraft used as example.

Specific	**Talon**	**DJI Phantom 4**	**DJI Inspire 2**	**Parrot Disco**	**DJI Mavic**	**Parrot Bepop**
Type	Fixed wing	Quad rotor	Quad rotor	Fixed wing	Quad rotor	Quad rotor
Mass (kg)	3.75	1.4	4.25	0.75	0.7	0.5
Front area (m^2)	0.1	0.02	0.04	0.07	0.02	0.02
Radius (m)	0.88	0.2	0.4	0.575	0.2	0.25
Maximum flight time	1.25 h	20 min	25 min	45 min	20 min	25 min
Drag coefficient at ballistic descent	N(0.9, 0.2)	N(0.7, 0.2)	N(0.7, 0.2)	N(0.9, 0.2)	N(0.7, 0.2)	N(0.7, 0.2)
Initial horizontal speed (m/s)	N(18, 2.5)	U(0, 15)	U(0, 20)	N(15, 2.5)	U(0, 15)	U(0, 15)
Initial vertical speed (m/s)	N(0, 1)	N(0, 1)	N(0, 1)	N(0, 1)	N(0, 1)	N(0, 1)
Glide speed (m/s)	16	7.5	10.0	12.0	7.5	7.5
Glide ratio	N(12, 2)	N(2.7, 0.8)	N(2.7, 0.8)	N(12, 2)	N(2.7, 0.8)	N(2.7, 0.8)
Drag coefficient at parachute descent	N(1.3, 0.2)	N(0.9, 0.2)	N(1.3, 0.2)	N(1.3, 0.2)	N(0.5, 0.2)	N(0.3, 0.2)
Parachute area (m^2)	1	0.5	1	0.5	0.5	0.5
Parachute deployment time (s)	2	2	2	2	2	2

Table 3 The event probabilities.

	Ballistic	**UG**	**Parachute**	**Fly away**
Event probability (per flight hour)	1/200	1/200	1/100	1/250

event probabilities assumed to compute the results are defined in Table 3. In order to demonstrate how the risk differs with the aircraft specifications, the event probabilities are the same for every vehicle type.

5.2 Talon aircraft

The first vehicle taken into account is the Heliscope Talon, a fixed wing aircraft. The risk map and event maps for each descent event type are illustrated in Figure 17, while the maximum, minimum and average risk values for each descent event type are reported in Table 8.

It can be noted how risk-values are effected by the population density. In fact the highest risk-values are located in the most populated area, while the south-east area is poorly populated and it is the area with minimum risk values. With the Talon aircraft predominant risk values are determined by ballistic and the uncontrolled glide events. The main reasons are the mass of the vehicle, the high cruise speed assumed as the initial speed and the high glide speed. With the parachute descent event the risk is reduced, but it remains considerable because of the mass of the vehicle and the effect of the wind. In fact the wind increases the horizontal velocity during the descent of the vehicle and, as a consequence, the kinetic energy at impact increases, as well as the probability of fatality. Risk values of the fly away event are equal in all the map. This happens because the 2D PDF covers a wide area and the resulting values of expected population density and sheltering factor are the same for each element of the map. However, the risk value of the fly away event contributes to define the minimum risk level in the risk map.

In order to ensure an appropriate level of safety, the risk of a flight operation should be lower than a *maximum acceptable risk.* According to [17,31], a suitable and conservative "Equivalent Level of Safety" is $1 \cdot 10^{-6}$ h^{-1}. As a consequence, the Talon aircraft is not appropriate to perform flight operations in urban environments because of the high risk level. In fact, the minimum risk value in the risk map is $4.409 \cdot 10^{-5}$ h^{-1}, then, there are no area where the flight is allowed.

As already mentioned, the risk map can be used to generate safe flight operations. In order to demonstrate it, in this work, we generate a minimum risk path, taking into account the risk map. The minimum risk path is computed using the Optimal Rapidly-exploring Random Tree (RRT*) [39] algorithm. RRT* is a sample-based algorithm that explores the search space with an incremental tree, minimizing the motion cost. In order to search for the minimum risk path, in this test, RRT* minimizes risk-values in the risk map. The resulting path is illustrated on the risk map of Figure 17, while Figure 18 reports the evolution of the risk along the path. The average risk value of the path confirms that the Talon is not suitable to perform flight operations in this area.

5.3 Phantom aircraft

The second vehicle is the DJI Phantom 4, a quad rotor aircraft. The risk map and the event maps for each descent event type are illustrated in Figure 19, while numerical results are reported in Table 4.

With the Phantom aircraft the resulting risk level is lower than the Talon one. Risk values of the ballistic descent are a decade lower, because of the lower mass and the dimension of the vehicle. The risk level associated to the uncontrolled glide event is drastically reduced. The main reason is the different behavior of the quad rotor configuration compared to the fixed wing one. The glide velocity is lower, as well as the glide angle in the uncontrolled glide descent. With the parachute descent event the risk is null. This happens because the kinetic energy at impact is lower than the threshold imposed by the Equation (8). In particular, due to the mass of the vehicle, the resulting descent speed of the vehicle is very low. With the parachute descent, the risk can be increased only by the wind speed. In fact, with high values of the wind speed, the kinetic energy at impact increases, exceeding the fatality threshold. The fly away event assumes low values of risk. With the Phantom aircraft the area involved by the PDF of the fly away event is smaller than the Talon aircraft one. For this reason the resulting risk level is variable in the map.

The risk map of Figure 19 shows that with the Phantom aircraft the resulting risk is governed by the ballistic descent event. However, the average risk value is still greater than the maximum acceptable risk and, considering the risk map, the flight is allowed only in little areas, i.e. where there are low values of population density.

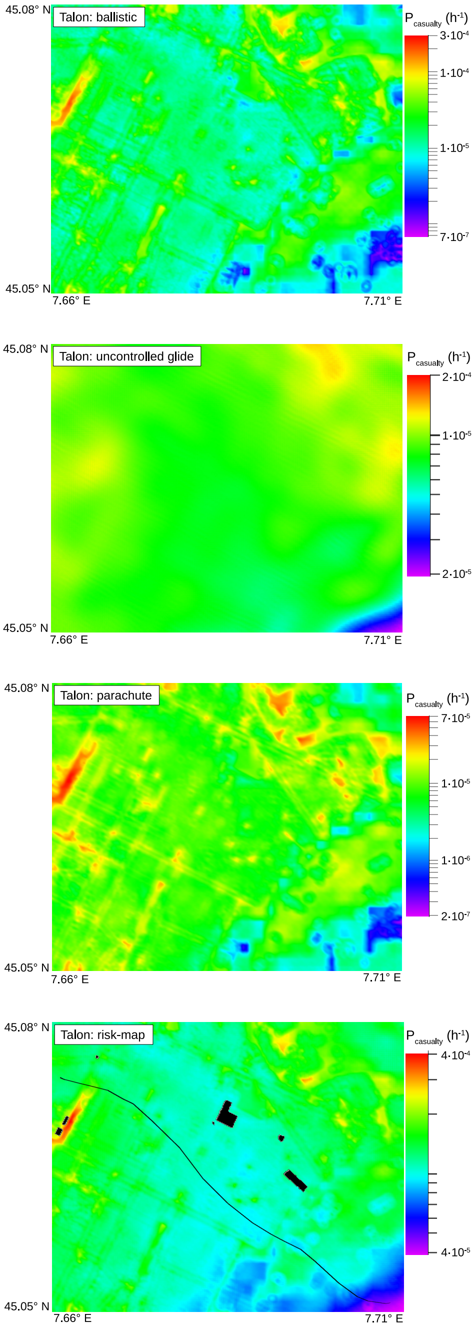

Fig. 17 Event maps and the risk map with the Talon aircraft. The event map of the fly away event is not reported because all elements have a constant value. On the risk map is also reported the minimum risk path computed to demonstrate the potential of the risk map. In all examples the flight altitude is $N(50, 5)$ m and wind with direction of -0.52 rad and speed $N(5, 1)$ m/s. Parameters of Talon aircraft are reported in Table 2.

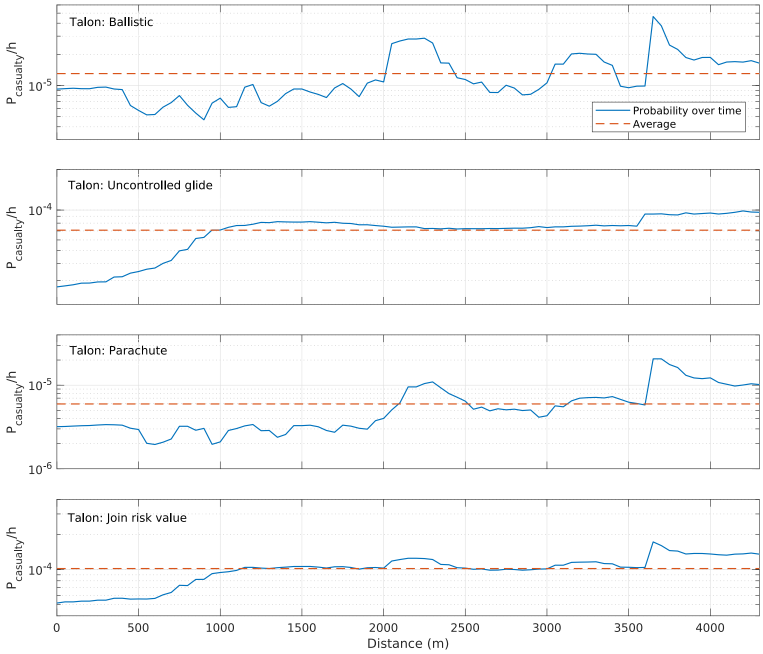

Fig. 18 The distribution of the probability of casualty $P_{casualty}$ along the minimum risk path with the Talon aircraft. The probability for each descent event type and the risk map are reported. The fly away event is not reported and has a constant value of $1.215 \cdot 10^{-5}\ h^{-1}$.

5.4 Other vehicles

In order to demonstrate the different behavior of the risk map, also other vehicles are considered: the DJI Inspire 2, the Parrot Disco, the DJI Mavic and the Parrot Bepop. Numerical results are reported in Table 4.

The DJI Inspire 2 is a quad rotor aircraft widely used by professional operators, because of its versatility and payload capacity. Due to the mass and dimensions, this aircraft is not suitable to fly in urban areas, because the resulting risk is always over the ELOS threshold.

The Parrot Disco is a fixed wing aircraft. Due to the low mass, the risk with the ballistic descent is low, as well as the null risk with the parachute descent. However, because of the high glide speed, the risk with the uncontrolled glide event is significantly.

The Mavic and the Bepop are quad rotor aircraft. With both vehicles the risk values of the risk map are defined only by the ballistic descent event, because with the other descent event types the risk is null. In both risk maps, there are a some areas where the risk is lower than $1 \cdot 10^{-6}$, thus, the fight is allowed. To demonstrate it, we compute the minimum risk path considering the Parrot Bepop aircraft. The risk map with the computed path is reported in Figure 20, while the evolution of the risk along the path is illustrated in Figure 21. The minimum risk path is also compared with the line of sight path

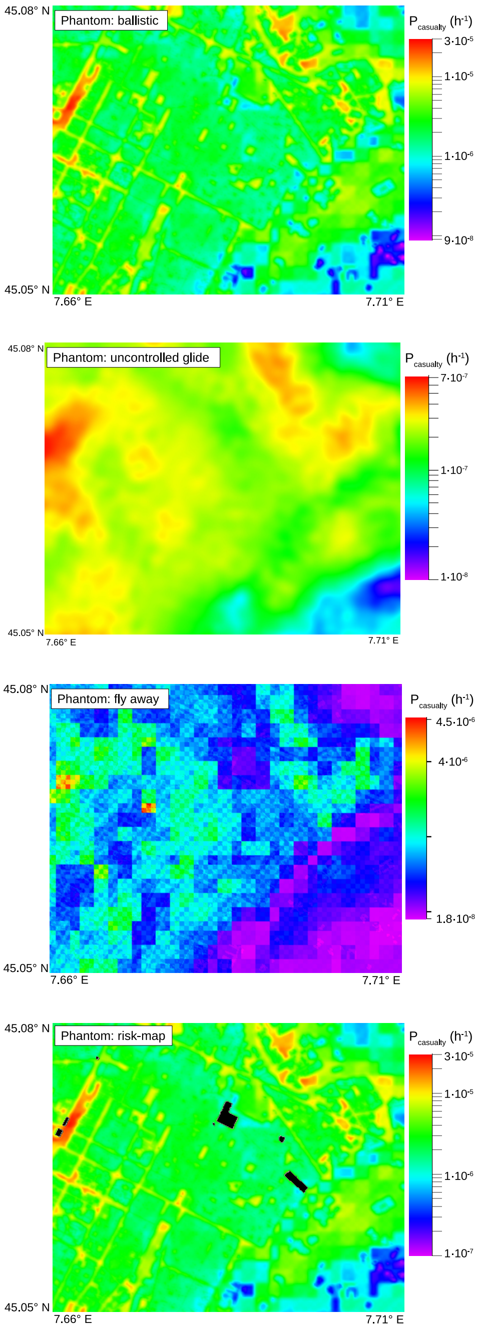

Fig. 19 Event maps and the risk map with the Phantom aircraft. The parachute descent is not reported because the risk is null for all elements in the map. In all examples the flight altitude is $N(50, 5)$ m and wind with direction of -0.52 rad and speed $N(5, 1)$ m/s. Parameters of Phantom aircraft are reported in Table 2.

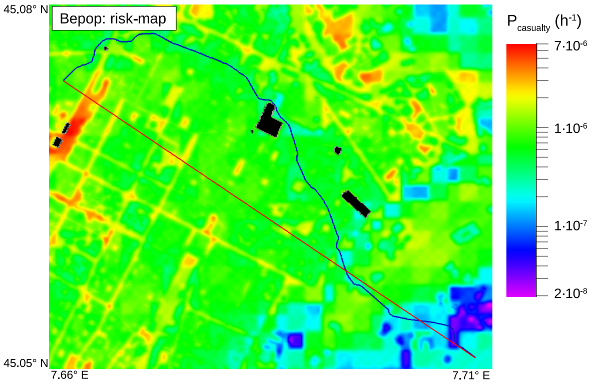

Fig. 20 The risk map with the Bepop aircraft. On the risk map is also illustrated the minimum risk path.

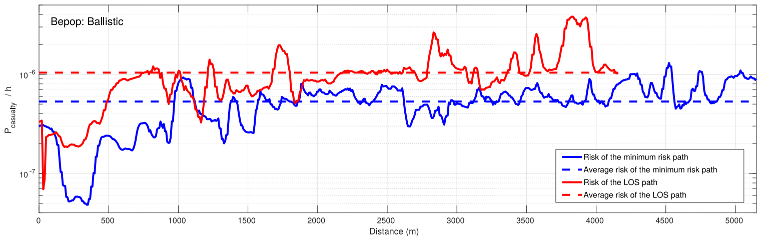

Fig. 21 The distribution of the probability of casualty along the minimum risk path of Figure 20 with the Bepop aircraft.

from the start to the target position. This test shows that with the Bepop aircraft the flight is safe, because the average risk is about $5 \cdot 10^{-7}$, lower than the Equivalent Level of Safety required by the National aviation agencies.

5.5 Discussion

The presented results show that the risk map is able to quantify the risk to the population of a wide urban area. In particular, the risk value computed for each element $P_{\text{casualty}}(x, y)$ in the map considers the risk of flight over the location (x, y). The proposed method assumes the failure happens in (x, y), then, it estimates the impact area using drone parameters and taking into account four descent event types, as well as uncertainties and the wind. Differently, the risk maps presented in [31, 48] compute the risk to the population assuming that the aircraft impacts in the location associated to the risk map element, without consider the behavior of the vehicle during the descent.

The proposed risk map can be used for ensuring risk-informed decision making. As illustrated in results, the risk map is able to detect the area where the flight is allowed or not, assuming a particular aircraft and its characteristics. For instance, taking into account the ELOS of $1 \cdot 10^{-6}$ h^{-1}, only

Table 4 Probabilities of casualty per flight hours for all risk maps.

Vehicle		**Ballistic**	**Uncontrolled glide**	**Parachute**	**Fly away**	**Final risk**
Talon	min	$7.668 \cdot 10^{-7}$	$2.009 \cdot 10^{-7}$	$2.994 \cdot 10^{-7}$	$1.216 \cdot 10^{-5}$	$4.409 \cdot 10^{-5}$
	max	$2.007 \cdot 10^{-4}$	$1.382 \cdot 10^{-4}$	$6.971 \cdot 10^{-5}$	$1.216 \cdot 10^{-5}$	$3.791 \cdot 10^{-4}$
	av	$1.124 \cdot 10^{-5}$	$8.840 \cdot 10^{-5}$	$1.001 \cdot 10^{-5}$	$1.216 \cdot 10^{-5}$	$1.318 \cdot 10^{-4}$
Phantom	min	$9.468 \cdot 10^{-8}$	$1.642 \cdot 10^{-8}$	0	$1.863 \cdot 10^{-8}$	$1.410 \cdot 10^{-7}$
	max	$2.699 \cdot 10^{-5}$	$6.556 \cdot 10^{-7}$	0	$4.409 \cdot 10^{-8}$	$2.758 \cdot 10^{-5}$
	av	$3.054 \cdot 10^{-6}$	$2.270 \cdot 10^{-7}$	0	$2.939 \cdot 10^{-8}$	$3.310 \cdot 10^{-6}$
Inspire	min	$4.515 \cdot 10^{-7}$	$6.670 \cdot 10^{-7}$	$1.502 \cdot 10^{-7}$	$8.519 \cdot 10^{-7}$	$2.390 \cdot 10^{-6}$
	max	$1.125 \cdot 10^{-4}$	$2.473 \cdot 10^{-5}$	$3.785 \cdot 10^{-5}$	$1.291 \cdot 10^{-6}$	$1.661 \cdot 10^{-4}$
	av	$1.220 \cdot 10^{-5}$	$7.372 \cdot 10^{-6}$	$5.141 \cdot 10^{-6}$	$1.007 \cdot 10^{-6}$	$2.572 \cdot 10^{-5}$
Disco	min	$2.867 \cdot 10^{-8}$	$9.254 \cdot 10^{-7}$	0	$4.941 \cdot 10^{-7}$	$1.846 \cdot 10^{-6}$
	max	$8.506 \cdot 10^{-6}$	$9.085 \cdot 10^{-6}$	0	$1.096 \cdot 10^{-6}$	$1.738 \cdot 10^{-5}$
	av	$1.294 \cdot 10^{-6}$	$6.104 \cdot 10^{-6}$	0	$6.693 \cdot 10^{-7}$	$8.079 \cdot 10^{-6}$
Mavic	min	$4.068 \cdot 10^{-8}$	0	0	0	$4.068 \cdot 10^{-8}$
	max	$1.089 \cdot 10^{-5}$	0	0	0	$1.089 \cdot 10^{-5}$
	av	$1.402 \cdot 10^{-6}$	0	0	0	$1.402 \cdot 10^{-6}$
Bepop	min	$2.609 \cdot 10^{-8}$	0	0	0	$2.609 \cdot 10^{-8}$
	max	$6.897 \cdot 10^{-6}$	0	0	0	$6.897 \cdot 10^{-6}$
	av	$9.714 \cdot 10^{-7}$	0	0	0	$9.714 \cdot 10^{-7}$

lightweight and small aircraft are allowed to fly in the city center of Turin. Moreover, results show that the fixed wing configuration involves more risk because of the high speed during the uncontrolled glide descent.

For this reason, the risk map can be used by operators to define or modify the flight mission of unmanned aircraft in urban areas. On the contrary, the proposed approach can be used by National aviation agencies as a tool to assess the risk of a particular flight operation and to provide the permission to fly. In order to meet requirements of National aviation authorities, the risk can be computed assuming the worst flight conditions, such as maximum velocities and altitude. The resulting risk may be conservative, but it guarantees that the ELOS requirement is satisfied. Moreover, according to [16], the probabilistic risk assessment approach seems to be largely in agreement with the SORA approach adopted by EASA.

The risk map can be used by a risk-aware path planning algorithm to seek for a low risk path. As showed, considering a particular flight operation, the Talon aircraft does not guaranteed the ELOS. On the contrary, considering the same start and goal positions, the Bepop aircraft is suitable to perform the flight mission, guaranteeing an average risk lower than $1 \cdot 10^{-6}$ h^{-1}. The risk-aware path planning is able to minimize the risk of a flight mission. In fact, the minimum risk path in Figure 20 involves lower risk than the line of sight path. The combination of risk map and risk-aware path planner allows a safe path to be planned.

6 Conclusions

In this paper, we propose the use of risk map in order to define the risk associated to unmanned aircraft in urban areas. The risk map is able to quantify the risk to the population on ground, when the UAS flies over a specified area.

The risk value is computed with a probabilistic risk assessment approach, taking into account drone specifications, environmental characteristic, as well as uncertainties on parameters ad wind. It considers different descent event types, such as ballistic descent, uncontrolled glide, parachute descent and fly away. Using the descent models, the probabilistic impact area is computed.

The risk map is generated combining several layers, containing specific information about the urban environment, such as the population density and the sheltering factor layer. It is also able to identify areas where the flight is forbidden because of no-fly zones forced by the National aviation agencies or the presence of obstacle at the flight altitude.

The simulation results show some examples of risk maps considering various vehicle models. The resulting map is able to quantify the risk over an entire urban area and with a desired resolution. Moreover, as demonstrated in the results, the risk map helps to search for the minimum risk path defining the expected risk of the flight mission.

The risk map is a tool for ensuring risk-informed decision making. It can be used to quantify the risk of a specific drone, determining if it is suitable to perform safe flight operations over urban areas.

In this paper, the risk map quantifies the ground risk. However, also the risk related to mid-air collision can be included in the risk-map. Future works include the improvement of the method, considering more descent events, as well as more types of aircraft.

Acknowledgements This work was supported by a fellowship from TIM, by the Siebel Energy Institute, and by Compagnia di San Paolo, Italy.

References

1. Ancel, E., Capristan, F.M., Foster, J.V., Condotta, R.C.: Real-time risk assessment framework for unmanned aircraft system (uas) traffic management (utm). In: 17th AIAA Aviation Technology, Integration, and Operations Conference, p. 3273 (2017)
2. Andreev, I., Hittenberger, M., Hofer, P., Kromp-Kolb, H., Kromp, W., Seibert, P., Wotawa, G.: Risks due to beyond design base accidents of nuclear power plants in europe—the methodology of riskmap. Journal of Hazardous Materials **61**(1), 257 – 262 (1998). DOI 10.1016/S0304-3894(98)00130-7
3. Arterburn, D., Ewing, M., Prabhu, R., Zhu, F., Francis, D.: FAA UAS Center of Excellence Task A4 : UAS Ground Collision Severity Evaluation. Tech. rep. (2017)
4. Bertrand, S., Raballand, N., Viguier, F., Muller, F.: Ground risk assessment for long-range inspection missions of railways by uavs. In: ICUAS 2017, International Conference on Unmanned Aircraft Systems, pp. 1343–1351. IEEE (2017). DOI 10.1109/ICUAS.2017.7991331
5. Bir, C., Viano, D.C.: Design and injury assessment criteria for blunt ballistic impacts. Journal of Trauma and Acute Care Surgery **57**(6), 1218–1224 (2004)
6. Bradski, G.: The OpenCV Library. Dr. Dobb's Journal of Software Tools (2000)

7. Capello, E., Dentis, M., Mascarello, L.N., Primatesta, S.: Regulation analysis and new concept for a cloud-based uav supervision system in urban environment. In: RED-UAS 2017, Workshop on Research, Education and Development of Unmanned Aerial Systems, pp. 90–95. IEEE (2017). DOI 10.1109/RED-UAS.2017.8101649
8. Castagno, J., Ochoa, C., Atkins, E.: Comprehensive risk-based planning for small unmanned aircraft system rooftop landing. In: ICUAS 2018, International Conference on Unmanned Aircraft Systems. IEEE (2018)
9. Clare, V.R., Lewis, J.H., Mickiewicz, A.P., Sturdivan, L.M.: Blunt trauma data correlation. Tech. rep., Edgewood Arsenal Aberdeen Proving Ground Md (1975)
10. Clothier, R.A., Walker, R.A.: Safety risk management of unmanned aircraft systems. In: Handbook of Unmanned Aerial Vehicles, pp. 2229–2275. Springer (2015)
11. Clothier, R.A., Walker, R.A., Fulton, N., Campbell, D.A.: A casualty risk analysis for unmanned aerial system (uas) operations over inhabited areas. In: AIAC12, Twelfth Australian International Aerospace Congress, 2nd Australasian Unmanned Air Vehicles Conference, pp. 1–15 (2007)
12. Clothier, R.A., Williams, B.P., Hayhurst, K.J.: Modelling the risks remotely piloted aircraft pose to people on the ground. Safety science **101**, 33–47 (2018). DOI 10.1016/j.ssci.2017.08.008
13. la Cour-Harbo, A.: Ground impact probability distribution for small unmanned aircraft in ballistic descent. preprint **-**, 1–24 (2017)
14. la Cour-Harbo, A.: Mass threshold for ‘harmless’ drones. International Journal of Micro Air Vehicles **9**(2), 77–92 (2017). DOI 10.1177/1756829317691991
15. la Cour-Harbo, A.: Quantifying ground impact fatality rate for small unmanned aircraft. Journal of Intelligent & Robotic Systems **-**, 1–18 (2018). DOI 10.1007/s10846-018-0853-1
16. la Cour-Harbo, A.: The value of step-by-step risk assessment for unmanned aircraft. In: ICUAS 2018, International Conference on Unmanned Aircraft Systems. IEEE (2018)
17. Dalamagkidis, K., Valavanis, K.P., Piegl, L.A.: On integrating unmanned aircraft systems into the national airspace system: issues, challenges, operational restrictions, certification, and recommendations, vol. 54. Springer Netherlands (2012)
18. De Filippis, L., Guglieri, G., Quagliotti, F.: A minimum risk approach for path planning of uavs. Journal of Intelligent & Robotic Systems **61**(1-4), 203–219 (2011). DOI 10.1007/s10846-010-9493-9
19. Denney, E., Pai, G., Whiteside, I.: Modeling the safety architecture of uas flight operations. In: International Conference on Computer Safety, Reliability, and Security, pp. 162–178. Springer (2017). DOI 10.1007/978-3-319-66266-4_11
20. Deville, P., Linard, C., Martin, S., Gilbert, M., Stevens, F.R., Gaughan, A.E., Blondel, V.D., Tatem, A.J.: Dynamic population mapping using mobile phone data. Proceedings of the National Academy of Sciences **111**(45), 15888–15893 (2014). DOI 10.1073/pnas.1408439111
21. Dey, P.K.: Managing project risk using combined analytic hierarchy process and risk map. Appl. Soft Comput. **10**(4), 990–1000 (2010). DOI 10.1016/j.asoc.2010.03.010
22. DJI: Phantom 4 - DJI’s smartest flying camera ever. `https://www.dji.com/en/phantom-4`. Accessed: 2019-01-28
23. Doxsey-Whitfield, E., MacManus, K., Adamo, S.B., Pistolesi, L., Squires, J., Borkovska, O., Baptista, S.R.: Taking advantage of the improved availability of census data: a first look at the gridded population of the world, version 4. Applied Geography **1**(3), 226–234 (2015). DOI 10.1080/23754931.2015.1014272
24. EASA: Certification specifications and acceptable means of compliance for large aeroplanes cs-25. Tech. rep., Amendment 21, European Aviation Safety Agency (2018)
25. EASA, European Aviation Safety Agency: Concept of Operations for Drones: A Risk Based Approach to Regulation of unmanned Aircraft. Cologne, Germany (2015)
26. European Aviation Safety Agency: Notice of proposed amendment 2017-05 (a) - introduction of a regulatory framework for the operation of drones. Tech. rep. (2017)
27. European Aviation Safety Agency: Notice of proposed amendment 2017-05 (b) - introduction of a regulatory framework for the operation of drones. Tech. rep. (2017)
28. FAA, Federal Aviation Administration: UAS Integration Pilot Program. `https://www.faa.gov/uas/programs_partnerships/uas_integration_pilot_program/`. Accessed: 2019-01-28

29. FAA, Federal Aviation Administration: System safety handbook. Department of transportation, Washington DC, USA (2000)
30. Fankhauser, P., Hutter, M.: A Universal Grid Map Library: Implementation and Use Case for Rough Terrain Navigation. In: A. Koubaa (ed.) Robot Operating System (ROS) – The Complete Reference (Volume 1), chap. 5. Springer (2016). DOI 10.1007/978-3-319-26054-9_5
31. Guglieri, G., Lombardi, A., Ristorto, G.: Operation oriented path planning strategies for rpas. American Journal of Science and Technology **2**(6), 1–8 (2015)
32. Guglieri, G., Quagliotti, F., Ristorto, G.: Operational issues and assessment of risk for light uavs. Journal of Unmanned Vehicle Systems **2**(4), 119–129 (2014)
33. Guglieri, G., Ristorto, G.: Safety assessment for light remotely piloted aircraft systems. In: INAIR 2016, International Conference on Air Transport, pp. 1–7 (2016)
34. Haartsen, Y., Aalmoes, R., Cheung, Y.: Simulation of unmanned aerial vehicles in the determination of accident locations. In: ICUAS 2016, International Conference on Unmanned Aircraft Systems, pp. 993–1002. IEEE (2016). DOI 10.1109/ICUAS.2016.7502548
35. Istat: Rapporto URBES 2015. `https://www.istat.it/storage/urbes2015/torino.pdf` (2015). Accessed: 2019-01-28
36. JARUS: Jarus guidelines on specific operations risk assessment (SORA), joint authorities for rulemaking of unmanned systems JARUS. Tech. rep. (2017)
37. Jensen, O.B.: Drone city-power, design and aerial mobility in the age of "smart cities". Geographica Helvetica **71**(2), 67 (2016). DOI 10.5194/gh-71-67-2016
38. Kang, C., Liu, Y., Ma, X., Wu, L.: Towards estimating urban population distributions from mobile call data. Journal of Urban Technology **19**(4), 3–21 (2012). DOI 10.1080/10630732.2012.715479
39. Karaman, S., Frazzoli, E.: Sampling-based algorithms for optimal motion planning. The International Journal of Robotics Research **30**(7), 846–894 (2011). DOI 10.1177/0278364911406761
40. La Cour-Harbo, A.: Quantifying risk of ground impact fatalities of power line inspection bvlos flight with small unmanned aircraft. In: Unmanned Aircraft Systems (ICUAS), 2017 International Conference on, pp. 1352–1360. IEEE (2017)
41. Lin, X., Fulton, N.L., Horn, M.E.: Quantification of high level safety criteria for civil unmanned aircraft systems. In: Aerospace Conference, pp. 1–13. IEEE (2014). DOI 10.1109/AERO.2014.6836463
42. Melnyk, R.V., Schrage, D.P., Volovoi, V., Jimenez, H.: A third-party casualty prediction model for uas operations. Georgia Institute of Technology (2012)
43. Michael, W., Luis, M., Jonathan, K., Xilin, Y., Felipe, G., Ben, U.: An automated emergency landing system for fixed-wing aircraft: Planning and control. Journal of Field Robotics **32**(8), 1114–1140. DOI 10.1002/rob.21641
44. Mohammed, F., Idries, A., Mohamed, N., Al-Jaroodi, J., Jawhar, I.: Uavs for smart cities: Opportunities and challenges. In: ICUAS 2014, International Conference on Unmanned Aircraft Systems, 2014, pp. 267–273. IEEE (2014). DOI 10.1109/ICUAS.2014.6842265
45. Naviair: Droneluftrum website. `https://www.droneluftrum.dk`. Accessed: 2019-01-28
46. OpenStreetMap contributors: Planet dump retrieved from https://planet.osm.org . `https://www.openstreetmap.org` (2017). Accessed: 2019-01-28
47. Primatesta, S., Capello, E., Antonini, R., Gaspardone, M., Guglieri, G., Rizzo, A.: A cloud-based framework for risk-aware intelligent navigation in urban environments. In: ICUAS 2017, International Conference on Unmanned Aircraft Systems, pp. 447–455. IEEE (2017). DOI 10.1109/ICUAS.2017.7991358
48. Primatesta, S., Guglieri, G., Rizzo, A.: A risk-aware path planning strategy for uavs in urban environments. Journal of Intelligent & Robotic Systems pp. 1–15 (2018)
49. Quigley, M., Conley, K., Gerkey, B., Faust, J., Foote, T., Leibs, J., Wheeler, R., Ng, A.Y.: Ros: an open-source robot operating system. In: ICRA workshop on open source software, vol. 3, p. 5 (2009)
50. Range Commanders Coucil: Standard 321-07 Common risk criteria standards for national test ranges: Supplement". USA Dept. of Defense (2007)

51. Rudnick-Cohen, E., Herrmann, J.W., Azarm, S.: Risk-based path planning optimization methods for unmanned aerial vehicles over inhabited areas. Journal of Computing and Information Science in Engineering **16**(2), 13 (2016). DOI 10.1115/1.4033235
52. Batista e Silva, F., Gallego, J., Lavalle, C.: A high-resolution population grid map for europe. Journal of Maps **9**(1), 16–28 (2013)
53. Smith, P.G.: Expected Casualty Calculations For Commercial Space Launch and Reentry Missions - Advisory Circular. Tech. rep. (2000)
54. Stöcker, C., Bennett, R., Nex, F., Gerke, M., Zevenbergen, J.: Review of the current state of uav regulations. Remote sensing **9**(5), 459 (2017)
55. Twisdale, L., Vickery, P.: Comparison of debris trajectory models for explosive safety hazard analysis. Tech. rep., Applied Research Associates Inc Raleigh Nc (1992)
56. Van Der Hoek, W., Konradsen, F., Amerasinghe, P.H., Perera, D., Piyaratne, M., Amerasinghe, F.P.: Towards a risk map of malaria for sri lanka: the importance of house location relative to vector breeding sites. International Journal of Epidemiology **32**(2), 280–285 (2003)
57. Washington, A., Clothier, R.A., Silva, J.: A review of unmanned aircraft system ground risk models. Progress in Aerospace Sciences (2017)
58. Washington, A., Clothier, R.A., Williams, B.P.: A bayesian approach to system safety assessment and compliance assessment for unmanned aircraft systems. Journal of Air Transport Management **62**, 18–33 (2017). DOI 10.1016/j.jairtraman.2017.02.003
59. Wu, P.P., Clothier, R.A.: The development of ground impact models for the analysis of the risks associated with unmanned aircraft operations over inhabited areas. In: Eleventh Probabilistic Safety Assessment and Management Conference (PSAM11) and the Annual European Safety and Reliability Conference (ESREL 2012), pp. 5222–5234 (2012)

Stefano Primatesta is currently a Ph.D. candidate in Computer and Control Engineering at the Politecnico di Torino, Italy. He received his B.S in Electronic Engineering end the M.S. in Mechatronic Engineering from Politecnico di Torino in 2011 and 2014, respectively. His research interests include autonomous navigation and service robotics, with applications on unmanned aerial vehicles and unmanned ground vehicles.

Alessandro Rizzo is an Associate Professor in the Department of Electronics and Telecommunications at Politecnico di Torino, Italy. He received the "Laurea" degree (summa cum laude) in computer engineering and the Ph.D. degree in automation and electronics engineering from the University of Catania, Italy, in 1996, and 2000, respectively. In 1998, he worked as EURATOM Research Fellow at JET Joint Undertaking, Abingdon, U.K., researching on sensor validation and fault diagnosis for nuclear fusion experiments. In 2000 and 2001, he worked as Research Consultant to ST Microelectronics, Catania Site, Italy, and as Industry Professor of Robotics at the University of Messina, Italy. From 2002 to 2015 he was a tenured Assistant Professor at Politecnico di Bari, Italy. In November 2015, he joined Politecnico di Torino. From 2012, he has also been a Visiting Professor at New York University Tandon School of Engineering, Brooklyn NY, USA. Prof. Rizzo is engaged in conducting and supervising research on complex networks and systems, modeling and control of nonlinear systems, cooperative robotics. He is author of two books, two international patents, and more than 130 papers on international journals and conference proceedings. Prof. Rizzo has been the recipient of the award for the best application paper at the IFAC world triennial conference in 2002 and of the award for the most read papers in Mathematics and Computers in Simulation (Elsevier) in 2009. Prof. Rizzo is also a Distinguished Lecturer of the IEEE Nuclear and Plasma Science Society.

Anders la Cour-Harbo is associate professor at Aalborg University, Department of Electronic Systems and Manager of AAU Drone Research Lab. He has a MSc in mathematics from 1998 and PhD in electronic engineering from 2002. His main research interests are guidance, control, modeling, and estimation of UAS, safety computations and operational safety for UAS, trajectory generation and flight operations in real environment. In addition, he is certified drone pilot, and routinely operates larger rotorcraft drones.